
Wesleyan University

Exploring the Role of Environment in the Composition of ONC Proplyds

by

Jonas Powell
Class of 2019

A thesis submitted to the
faculty of Wesleyan University
in partial fulfillment of the requirements for the
Degree of Master of Arts

Middletown, Connecticut

April, 2018

*If people sat outside and looked at the stars each night,
I'll bet they'd live a lot differently.*

—CALVIN & HOBBES

Contents

1	Analysis	1
1.1	Gas Model	1
1.1.1	Establishing Physical Profiles	2
1.1.2	Generating a Model Image	5
1.2	Exploring Parameter Space	6
1.2.1	Grid Search	7
1.2.2	Markov Chain Monte Carlo	8
1.3	Fitting Procedure	10
1.3.1	HCO ⁺ (4-3) Fit	13
1.3.2	HCN(4-3) Fit	13
1.3.3	CO(3-2) Fit	14
2	Discussion	25
2.1	Reflections on the Fits	25
2.2	Comparison with the Literature	27
2.3	Formation of the Binary	32
2.4	Planet-Forming Potential	32
	Bibliography	33

List of Figures

1.1	Since disk A and B's features are assumed to be independent, we may generate corner plots for each of their parameter spaces individually. Some analysis REWORK when new plots are added. REWORK: these are not the most recent ones	10
1.2	Moment-1 map of HCN emission, overlaid with ellipses described by each disk's best-fit position angle, inclination, and outer radius. For disk B, both the best-fit outer radius with and without the 220 AU a posteriori prior implemented (at 324 and 145 AU, respectively) are plotted.	15
1.3	Cornerplots of results from MCMC fitting of HCO^+ emission.	18
1.4	Channel maps of HCO^+ emission data, as well as a best-fit model from MCMC fitting and residuals from the two.	19
1.5	Cornerplots of results from MCMC fitting of HCN emission.	20
1.6	Channel maps of HCO^+ emission data, as well as a best-fit model from MCMC fitting and residuals from the two.	21
1.7	Cornerplots of results from MCMC fitting of HCN emission.	22
1.8	Channel maps of HCO^+ emission data, as well as a best-fit model from MCMC fitting and residuals from the two.	23
1.9	Density and temperature profiles for the best-fit models for CO, HCO^+ , and HCN.	24

2.1 Models from Walsh et al. (2013) showing radial and vertical distributions of CO, HCO⁺, and HCN in a simulated disk around a T-Tauri star, being radiated by a nearby O star. The top row shows the profiles of isolated disks (Walsh et al. 2010), while the bottom row shows the profiles of disks being irradiated by a nearby O star (Walsh et al. 2013). Note that bottom row is on a log scale and only covers the inner 100 AU of the disk, while the top row is linearly scaled and shows a 300AU stretch. *It seems like only having one of these sets of images would make more sense.* 31

Chapter 1

Analysis

By modeling spatially and spectrally resolved observations of protoplanetary disks, we can measure their chemical and physical characteristics. To model the system, we generate a synthetic image of what a disk with known physical characteristics (like disk radius, mass, and so on) would look like at a certain distance, inclination, and position angle relative to us. From that synthetic image, we may generate a synthetic set of visibilities, and then compare those visibilities to our observations. By iterating this process, we may generate many models with different parameter combinations and evaluate how well each resulting model disk matches our observations. We use a Markov Chain Monte Carlo technique described in §1.2.2 to explore the parameter space and measure the physical properties of the disk.

In §1.1, we describe the basic equations and computational processes that generate the model disks. In §1.2, we describe how, once models are made, we move through high-dimensional parameter space to identify regions of best-fit. Finally, in §2.4, we present the results of our fitting procedures.

1.1 Gas Model

In this work, we use a gas-disk model originally developed by (Rosenfeld et al. 2012, 2013) and translated from IDL to Python by Flaherty et al. (2015). The

code assumes that Local Thermal Equilibrium¹ (LTE), and hydrostatic equilibrium. The code draws on user-given temperature- and surface-density profiles to calculate a vertical density structure, and calculates the model disk’s velocity field based on the stellar mass. It then performs radiative transfer on the resulting structure to create a sky-projected image of the model disk, taking into account line thermal and turbulent line broadening. By assuming LTE and hydrostatic equilibrium, the code is able to run quickly enough to allow for a Markov Chain Monte Carlo routine to generate models on a reasonable timescale, as described in §1.2.2.

1.1.1 Establishing Physical Profiles

A circumstellar disk can be characterized by three major profiles: its radial and vertical temperature structures, its radial and vertical density structures, and its velocity field. Generating a model disk is a matter of defining these three functions.

For the disk’s temperature profile, our code uses the parametrization of disk temperature structure first laid out by Dartois et al. (2003), where the disk’s temperature is given by,

$$T_{\text{gas}}(r, z) = \begin{cases} T_a + (T_m - T_a) \left[\cos \frac{\pi z}{2z_q} \right]^{2\delta} & \text{if } z > z_q \\ T_a & \text{if } z \leq z_q(r). \end{cases} \quad (1.1)$$

The atmospheric temperature and mid-plane temperatures are given by $T_a =$

¹This may or may not be a valid assumption in protoplanetary disks, but Pavlyuchenkov et al. (2007) showed that it was appropriate for CO.

$T_{atm,150}(r/150\text{AU})^q$ and $T_m = T_{mid,150}(r/150\text{AU})^q$, where q is typically negative and controls the functions' decay. Since T_m is smaller than T_a , the second term of the low-scale height temperature function is negative, so the sinusoid effectively implements a decreasingly-negative contribution to the temperature with height above midplane. The disk's scale height, controlled by z_q , is assumed to be radially increasing, as described by a power law, $z_q(r) = z_{q,150}(r/150\text{AU})^{1.3}$. δ , a tunable exponent controlling the rate of the disk's vertical temperature decay, is set to 1 as in Factor et al. (2017), though it can take on values between 1-2 (Dartois et al. (2003)).

The disk's velocity field is assumed to be Keplerian with slight corrections for gas pressure support and the addition of a vertical dependence. The assumption of Keplerian velocities is generally valid in the case that $M_{\text{disk}} \ll M_*$, which continuum observations of the system have shown to be the case for the disks in this system. With these corrections added, the model disk's velocity field is given by

$$\frac{v_\phi^2}{r} = \frac{GM_*r}{(r+z)^{3/2}} + \frac{1}{\rho_{\text{gas}}} \frac{\partial P_{\text{gas}}}{\partial r}; \quad v_r = v_z = 0. \quad (1.2)$$

The final structure we would like to define is the disk's gas density profile. By assuming hydrostatic equilibrium, we may relate the disk's gas density and temperature profiles as

$$-\frac{\partial \ln \rho_{\text{gas}}}{\partial z} = \frac{\partial \ln T_{\text{gas}}}{\partial z} + \frac{1}{c_s^2} \left[\frac{GMz}{(r^2+z^2)^{3/2}} \right]. \quad (1.3)$$

Here c_s is the local sound speed, given by $c_s^2 = \frac{k_B T_{\text{gas}}}{\mu m_H}$, T_{gas} is the temperature profile given above, m_H the mass of hydrogen, and μ is the mean molecular weight of the gas, set here at 2.37 to reflect the gas's 80% H₂ composition. We may solve this equation by integration, giving us the disk's density profile $\rho(r, z)$.

The model's surface density profile is drawn from Hartmann et al. (1998), in which they expanded on the work of Lynden-Bell & Pringle (1974) to show that the structure of an isolated disk with viscosity given by $\nu \propto R^\gamma$ is well-described by

$$\Sigma_{\text{gas}}(r) = \frac{M_{\text{gas}}(2 - \gamma)}{2\pi R_c^2} \left(\frac{r}{R_c}\right)^{-\gamma} \exp\left[-\left(\frac{r}{R_c}\right)^{2-\gamma}\right], \quad (1.4)$$

where R_c is the radial extent of the gas disk, γ is a power law index, and M_{gas} is the total gas mass. This form allows the disk to behave as a power law radially until R_c , at which point it turns over into exponential decay. Hughes et al. (2008) showed that exponentially tapering the disk's outer radius, rather than sharply cutting it, provides the best agreement between gas and disk outer radii. We approximate $M_{\text{gas}} = M_{\text{disk}}$, since at this early stage in the disk's development, the gas is by far the majority element of the disk's mass total (although, as discussed in §???, this assumption has come under scrutiny in recent years).

Modifications are made to this density profile in two cases. At sufficiently low temperatures, molecules will condense out of the gas phase. The mid-plane of the disk is sufficiently cold to prompt this behavior. We may simulate this behavior by dropping the gas density by a factor of 10^{-18} wherever the temperature falls below some characteristic freeze-out temperature, T_{FO} , a temperature which is molecule-specific. Conversely, at the disk's upper surface, photodissociation by stellar and

Table 1.1: Molecule-specific values

Parameter	Description	Fixed Value(s)	
		CO, HCO ⁺	HCN
T _{FO}	Molecular freeze-out temperature	19	60
σ _{Max}	Column density upper limit	[1.3 × 10 ³⁰] cm ⁻²	9.5 × 10 ²¹ cm ⁻²

* Values drawn from Factor et al. (2017)

interstellar radiation dominates, so we implement a decrease in density wherever the hydrogen column density at the disk’s surface falls below a characteristic value. We use values drawn from Factor et al. (2017) for these parameters, presented in Table 1.1.

1.1.2 Generating a Model Image

Having now established our model disk’s physical structure through temperature, density, and velocity profiles, we may begin generating an image of the disk by calculating flux contributions through the disk. To do so, we calculate the specific intensity by integrating the equation of radiative transfer:

$$I_\nu = \int_0^\infty K_\nu(s) S_\nu(s) e^{-\tau_\nu(s)} ds, \quad (1.5)$$

where $K_\nu(s)$ is the absorption coefficient, $\tau_\nu(s)$ is the optical depth and is defined as $\tau_\nu(s) = \int_0^s K_\nu(s') ds'$, and $S_\nu(s)$ is the source function. Since disks emit as blackbodies, the Planck function, $B_\nu(T)$, is used as the source function. Line broadening, a function of temperature and disk turbulence, is added, and the resulting flux is Doppler shifted to account for the disk’s user-specified systemic velocity. Finally, the image is scaled, shifted, and rotated to account for the

source's distance (d), angular offset from the center of the image ($\Delta\alpha$ and $\Delta\delta$), and position angle and inclination (PA and i) relative to our viewing direction.

Since the model disk is fully defined at every point in both physical and velocity space, we may set the spatial and spectral resolution to ensure that it is sampled well compared to the resolution of the data. We set our spectral resolution to match that of our observation, while we let the spatial resolution be $\sim 1/10$ the size of the synthesized beam. This resolution is high enough to avoid sampling artifacts when we simulate interferometric observations of the image.

We then use the Miriad task `uvmodel` to generate visibilities from the model image, sampled in the same uv tracks as our observation. The χ^2 statistic is then used as a goodness-of-fit metric to compare the data and model in the visibility domain. We make this calculation in the visibility domain, rather than the image domain, so that the resulting χ^2 value is not influenced by artifacts generated in the imaging process.

In summary, we can generate a model disk by calculating its physical structures (in radial temperatures, densities, and velocities), then drawing on radiative transfer to calculate the flux contributions from the disk. That flux is sky-projected to match the observed source's orientation, and the resulting image is then transformed from the image domain to the visibility domain and its fit quality evaluated.

1.2 Exploring Parameter Space

Now that we have the tools available to generate synthetic images that are tuneable across a large number of parameters, we must decide how best to move through that large parameter space to find a best-fit region. To do so, we use two

methods.

1.2.1 Grid Search

The first, and perhaps most intuitive, way to move through this parameter space is using a simple grid search. A grid search involves manually assembling lists of values to try for each parameter and then generating models and calculating the resulting χ^2 value for every possible combination of parameters in those lists. A best-fit value is recovered by simply finding the point in that n -dimensional grid that yielded the best χ^2 , and then either calling that position in parameter space a best-fit location or then defining a finer grid around that point and repeating the process until an acceptable resolution has been reached. Benefits of grid search include its relatively straightforward nature (and, consequentially, the relative simplicity of implementing it) and its usefulness as a diagnostic tool, since very specific regions of parameter space may be sampled with the manual entry of positions to test. However, it is a relatively simple method and leaves room for improvement.

Grid search was used to locate the disks in (α, δ, v) space. All other parameters were fixed at best-guessed values, then grids were run with resolutions sufficiently fine to meet the observations' spatial and spectral resolution. Grids for the disks' systemic velocities were centered at values found in Williams et al. (2014), while $\Delta\alpha$ and $\Delta\delta$ offsets were first approximated using the MIRIAD task **uvfit** to fit a Gaussian to each disk. The resulting centroids were used to center the grids for refinement.

1.2.2 Markov Chain Monte Carlo

Markov Chain Monte Carlo (MCMC) algorithms offer us a way to both sample the probability distribution of a high-dimensional parameter space (much like a grid search), but offers an improvement over grid search by yielding the posterior probability distribution of each point, which allows us to characterize the uncertainty associated with each best-fit value with error bars. We use an affine-invariant formulation of the MCMC algorithm described by Goodman & Weare (2010) and implemented in the Python package emcee by Foreman-mackey et al. (2013).

MCMC routines sample the probability distribution of a given n -dimensional parameter space by deploying an army of “walkers.” Each walker begins at some initial position, evaluates the χ^2 value of that point, and then proposes moving to a new position in parameter space according to a Gaussian probability distribution centered at the current point and decaying with distance (so that nearer points are preferentially, but not necessarily, selected). The χ^2 value of this new position - or “step” - is then evaluated, and is either accepted (the walker moves to that position) or rejected (the walker remains where it is and repeats the new-step proposal process) with probability $p = \exp [(\chi_{\text{current}}^2 - \chi_{\text{new}}^2)/2]$. This function indicates that if the proposed step yields a better fit (a lower χ^2 value) than the current position, $p > 1$ and the step is accepted. However, if proposed step results in a worse fit, there is still a non-zero chance that the step is accepted, proportional to how much worse it is. This willingness to accept an increased χ^2 value allows the walker to avoid becoming trapped in local minima. The list of steps taken by each walker and their accompanying χ^2 values are compiled into the “chain” part of Markov Chain Monte Carlo. Goodman & Weare (2010) show

that a walker’s desire to remain in near a certain position is proportional to that position’s local probability density, meaning that we may infer uncertainties in our fits from the density of walker steps taken in a region.

We may introduce boundaries to the parameter space explored by our walkers using “priors.” These priors are manually set, and allow us to restrict the walkers’ motions from entering regions that we know a priori to be implausible fits. Justifications for these constraints are either physical (e.g. a disk should not have a negative radius) or observed (e.g. both disks’ radii are clearly far less than 1000 AU). These priors may be either uniform, with hard cuts at their bounds, or Gaussian, with preferential treatment given to walkers closer to the Gaussian centroid (a known value). For this work, we implement a Gaussian prior on each disk’s position angle in order to guide the search towards the values reported in Williams et al. (2014) but still allow it the flexibility to self correct if necessary. This prior takes the form of a contribution to the log likelihood function, such that:

$$\text{lnprob} = -\chi/2 - \ln \frac{1}{\sqrt{2\pi\sigma_{PA}^2}} e^{-\frac{\text{PA}^2}{2\sigma_{PA}^2}} \quad (1.6)$$

for each disk’s position angle, where σ_{PA} is the position angle uncertainty given by Williams et al. (2014).

We may visualize the results of the walkers’ journeys using corner plots. Corner plots allow high-dimensional space to be visualized in two dimensions by taking slices across each pair of axes and showing the density of samples drawn in that slice. In each of these slices, a perfectly certain fit would appear as a very tight, point-like Gaussian - the sample density around the best fit would be extremely

high and low everywhere else, as the walkers quickly converged and remained on that best fit point - while conversely, higher uncertainties are shown by a wide spread of samples around the central point. Degeneracies between parameters can be seen as streaks in these corner plots, showing that a change in one parameter produces a change in the other. Corner plots for Disk A and B in an HCO⁺ fit are shown in Figs 1.1a and 1.1b, respectively.

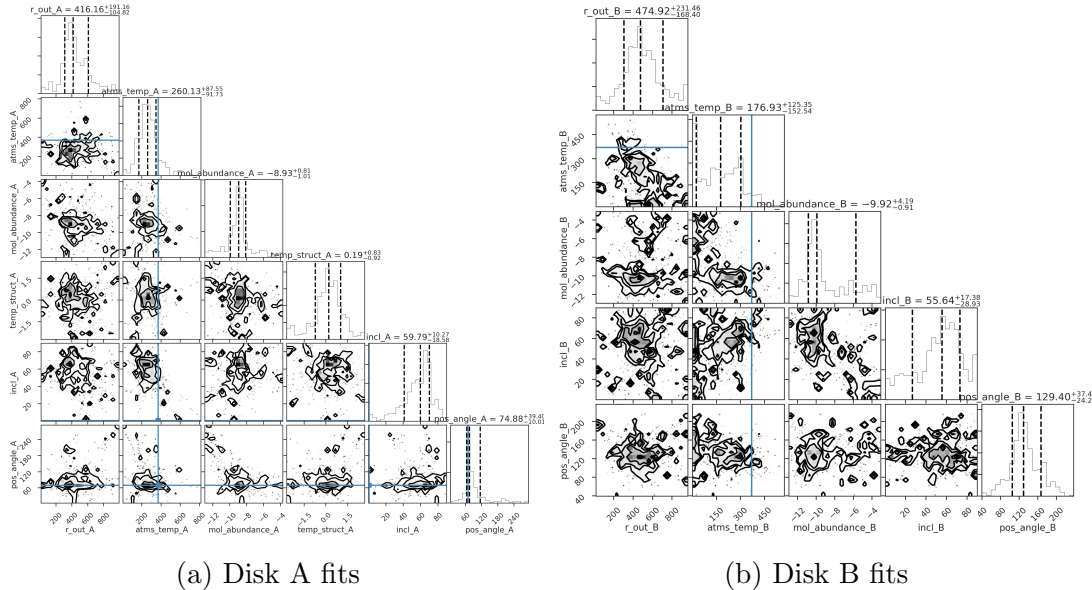


Figure 1.1: Since disk A and B's features are assumed to be independent, we may generate corner plots for each of their parameter spaces individually. Some analysis REWORK when new plots are added. REWORK: these are not the most recent ones

1.3 Fitting Procedure

Fitting of the data began with the analysis and partial removal of cloud contamination discussed in Section ??, resulting in the removal of baselines below a characteristic length for each line. With the data as clean as possible, position ($\Delta\alpha, \Delta\delta$) and velocity (v_{sys}) offsets were fit for. Offset fitting was executed

only in the HCO⁺ line, thanks to the line's minimal contamination and high signal strength, and was performed as described in §1.2.1. With these values established, they were treated as fixed parameters for the remainder of the fitting process.

Table 1.2 presents a list of parameters, including α , δ , and v_{sys} , which were left fixed throughout the MCMC runs. Since we are only modeling one line at a time, we are unable to constrain the vertical temperature structure and so fix T_{mid} and z_q . The selection of midplane temperature was made following Factor et al. (2017) to reflect the "CO snow line" shown by Qi et al. (2011)², while the value of z_q was chosen, again following Factor et al. (2017), to be roughly double the disks' scale heights, as shown in Rosenfeld et al. (2013). Since HCO+ is optically thin, temperature and density are degenerate, so γ is set at 1 following Andrews et al. (2009), who showed this to be a reasonable value for disks in ρ Ophiuchus. Since our observations do not have enough spectral resolution to constrain the observations' turbulent linewidth, we fix v_{turb} at around 1% of the sound speed, per Williams et al. (2014).

In fitting the HCO⁺ and HCN emission, we fix M_{disk} at values drawn from Williams et al. (2014), which they infer from continuum flux measurements (and relying on the 100:1 gas/dust ratio discussed in §??).

The remaining parameters, presented and discussed in ??, are fit for using MCMC. We implement priors on each parameter, reported in Table 1.3. Gaussian priors are used for the fitting of both disks' position angles, centered at values reported by Williams et al. (2014).

The result from the MCMC runs are presented below. To facilitate easier reading, figures are found at the end of the chapter.

²Although their measurements were made for sources in a different environment, the value gives us a reasonable starting point for our fits.

Table 1.2: Fixed Parameter Values

Parameter	Description	Source	Fixed Value(s)	
			(Disk A)	(Disk B)
$\Delta\alpha$ ('')	RA offset from image center	0	0.0002	-1.006
$\Delta\delta$ ('')	Dec offset from image center	0	0.082	-0.3
v_{sys} (km s $^{-1}$)	Systemic velocity	0	10.00	10.75
i ()	Inclination	1	65	45
M_* (M_\odot)	Stellar mass	1	3.5	0.4
Log M_{disk} (M_\odot)	Disk gas mass [*]	1	-1.11	-1.55
v_{turb} (km s $^{-1}$)	Turbulence velocity	2		0.081
d (pc)	Distance	3		389
R_c (au)	Critical radius	1		100
γ	Radial density power law index	4		1
z_q (au)	Disk scale height at 150 AU	5		29
T_{mid} (K)	Midplane temp. at 150 AU	6		19

^{*} For the HCO⁺ and HCN lines, we fix disk gas mass, while in our CO fit, it is a fixed parameter.

⁰ Grid-search and/or elliptical fitting, as described in §1.2.1

¹ Williams et al. (2014)

² Flaherty et al. (2015)

³ Gaia Collaboration et al. (2018)

⁴ Andrews et al. (2009)

⁵ Factor et al. (2017)

⁶ Qi et al. (2011)

Table 1.3: Fit Parameter Values

Parameter	Description	Prior
X_{mol}	Molecular abundance, relative to H ₂ ^a	Uniform
q	Radial temperature power law index	Uniform
PA ^b (°)	Position Angle	Gaussian
T_{atms} (K)	Atmospheric temperature at 150 AU	Uniform
Log M_{Disk} (M_\odot)	Log Disk mass ^c	Log Uniform

^a For the CO line, X_{mol} is fixed at the literature value of 10⁻⁴.

^b In our CO fit, disk B's position angle, PA, is fixed at the best-fit value from the HCO⁺ fits.

^c For HCO⁺ and HCN, disk mass was fixed at values from Williams et al. (2014).

1.3.1 HCO⁺ (4-3) Fit

We began by fitting the HCO⁺line, using the MCMC methods explained above. Best fit and median values with $1-\sigma$ uncertainties are given in Table 1.4, while corner plots, showing the posterior distributions of the individual line fit, is shown in Fig. 1.3.

We see from the corner plots that, in general, the fits are quite well constrained. Uncertainties surrounding disk B's outer radius leads to some degeneracies, but overall this fit seems to be well managed. Inspection of the channel maps of the HCO⁺data, best-fit model, and residuals (Fig. 1.4) show that, while the model seems to reproduce the data's morphological structure fairly well, fluxes are systematically low, leaving significant residuals. This could be fixed, somehow.

Table 1.4: MCMC Fitting Results (HCO⁺)

Parameter	Disk A		Disk B	
	Median	Best Fit	Median	Best Fit
X _{mol}	$-n_{-0}^{+0.}$	-8.12	$-n_{-0}^{+0.}$	-10.3
r _{out} (au)	$-n_{-0}^{+0.}$	333.86	$-n_{-0}^{+0.}$	240.69
i (°)	$-n_{-0}^{+0.}$	[65]	$-n_{-0}^{+0.}$	[45]
PA (°)	$-n_{-0}^{+0.}$	69.79	$-n_{-0}^{+0.}$	121.22
q	$-n_{-0}^{+0.}$	0.77	$-n_{-0}^{+0.}$	[-0.5]
T _{atms} ()	$-n_{-0}^{+0.}$	172.95	$-n_{-0}^{+0.}$	183.17
lnprob			-28404.97	

* Values in [brackets] were fixed for this run.

1.3.2 HCN(4-3) Fit

We proceed by next modeling HCN using the same methods as for HCO⁺. As before, best fit and median values with $1-\sigma$ uncertainties are given in Table 1.6,

channel maps are presented in Fig. 1.6, and corner plots are shown in Fig. 1.5.

In the channel maps, we see that the fit is generally good, leaving fairly minimal residuals behind. The residuals do, however, highlight a stream of flux connecting the two disks, particularly at velocities around 9.4-10.2 km/s that our model is unable to fit. This stream is most visible in the HCN line, compared to the HCO⁺and CO maps.

For both disks, the posterior distribution of fits to outer radius is bimodal. This likely is a result of the MCMC walkers struggling to make sense of the above-mentioned bridge between the disks. This is particularly the case with disk B, where the walkers are distributed around 100 AU and around 350 AU. As a test, we can remove all steps in the MCMC chain where disk B's outer radius exceeds 220 AU (which is somewhere in the middle of the bimodality in the parameter's posterior distribution, but is still appreciably higher than the HCO⁺fit value of ~ 150 AU). Doing so brings HCO⁺and HCN into almost perfect agreement ($< 1\%$) on disk B's outer radius, while also increasing disk A's HCN abundance by more than an order of magnitude and pushing disk B's temperature up to more than twice the value found for the HCO⁺line. See Table ?? for a selection of the fit parameters, selected based on whether they change with the radius cut. Fig 1.2

Otherwise, the posteriors are widely unimodal. There are no particularly noticeable degeneracies between parameters.

1.3.3 CO(3-2) Fit

Finally, we fit the CO(3-2) line. Despite the removal of baselines below 60 $k\lambda$, the CO(3-2) line still shows significant cloud contamination in channels near the systemic velocity (Fig. 1.8). In an attempt to keep the MCMC walkers from

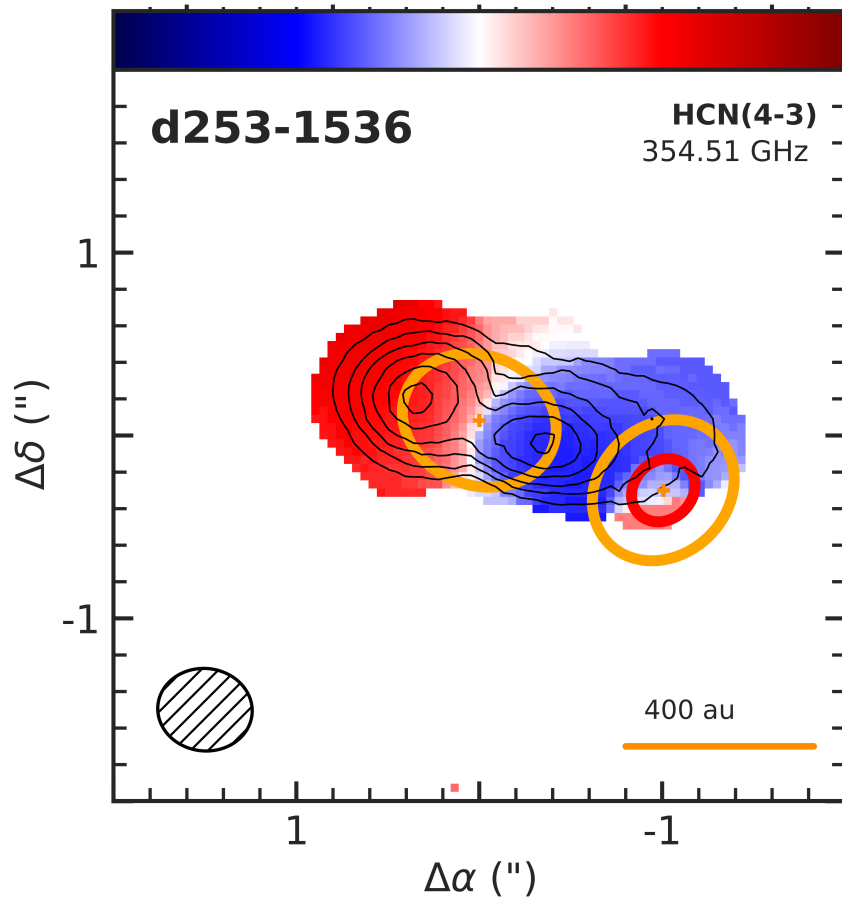


Figure 1.2: Moment-1 map of HCN emission, overlaid with ellipses described by each disk's best-fit position angle, inclination, and outer radius. For disk B, both the best-fit outer radius with and without the 220 AU a posteriori prior implemented (at 324 and 145 AU, respectively) are plotted.

Table 1.5: MCMC Fitting Results (HCN)

Parameter	Disk A		Disk B	
	Median	Best Fit	Median	Best Fit
X _{mol}	-n _{-0.} ^{+0.}	-7.87	-n _{-0.} ^{+0.}	-11.09
r _{out} (au)	-n _{-0.} ^{+0.}	334.48	-n _{-0.} ^{+0.}	292.37
i (°)	-n _{-0.} ^{+0.}	[65]	-n _{-0.} ^{+0.}	[45]
PA (°)	-n _{-0.} ^{+0.}	70.05	-n _{-0.} ^{+0.}	134.2
q	-n _{-0.} ^{+0.}	0.62	-n _{-0.} ^{+0.}	[-0.5]
T _{atms} ()	-n _{-0.} ^{+0.}	125.68	-n _{-0.} ^{+0.}	388.21
ln Likelihood			-30928.35	

* Values in [brackets] were fixed for this run.

Table 1.6: MCMC Fitting Results (HCN),
R_{out} < 220

	X _{mol}	r _{out} (au)	q	T _{atms} ()
Disk A	-6.98	337.57	0.89	86.13
Disk B	-10.3	145.57	[-0.5]	281.89

trying to fit the contamination, we remove the channels with velocities between 9.88 and 12 km s⁻¹, which show the worst of the clouds' effects. By choosing to not include these, we sacrifice some data, but the resulting fits are more representative of the structures we care about - the disks themselves - than they would be had we not sacrificed those channels. In retrospect, it is likely that it would have been preferable to exclude a far wider range of contaminated channels, likely from around 6.5-13.3 km/s.

Consequentially, the resulting fits are noticeably less certain than those of the HCO+ and HCN lines, featuring several jagged and bimodal posteriors, shown in Fig. 1.7. Additionally, since the best-fit values disagree significantly with the results from the other lines (particularly in the T_{atms} for disk A, which is

Table 1.7: MCMC Fitting Results (CO)

Parameter	Disk A		Disk B	
	Median	Best Fit	Median	Best Fit
$\log M_{\text{Disk}}$ (M_{\odot})	$-n_{-0.}^{+0.}$	-0.29	$-n_{-0.}^{+0.}$	-4.9
r_{out} (au)	$-n_{-0.}^{+0.}$	437.71	$-n_{-0.}^{+0.}$	261.13
i ($^{\circ}$)	$-n_{-0.}^{+0.}$	65	$-n_{-0.}^{+0.}$	45
PA ($^{\circ}$)	$-n_{-0.}^{+0.}$	66.73	$-n_{-0.}^{+0.}$	[136]
q	$-n_{-0.}^{+0.}$	0.28	$-n_{-0.}^{+0.}$	[-0.5]
T_{atms} (K)	$-n_{-0.}^{+0.}$	5.54	$-n_{-0.}^{+0.}$	177.15
ln Likelihood			-33597.46	

* Values in [brackets] were fixed for this run.

unrealistically low), we are unable to include these results in our analysis.

Interestingly, the CO line seems to have had some marginal success in recovering disk radii, returning a best-fit value disk B that is within <10% of the HCO⁺line's reported value, and, although the best-fit radius for disk A is unreasonably high at nearly 500 AU, the 50th percentile fit is within 15% of the HCO⁺value. This seems to indicate that these data still have potential value if constrained appropriately.



Figure 1.3: Cornerplots of results from MCMC fitting of HCO^+ emission.

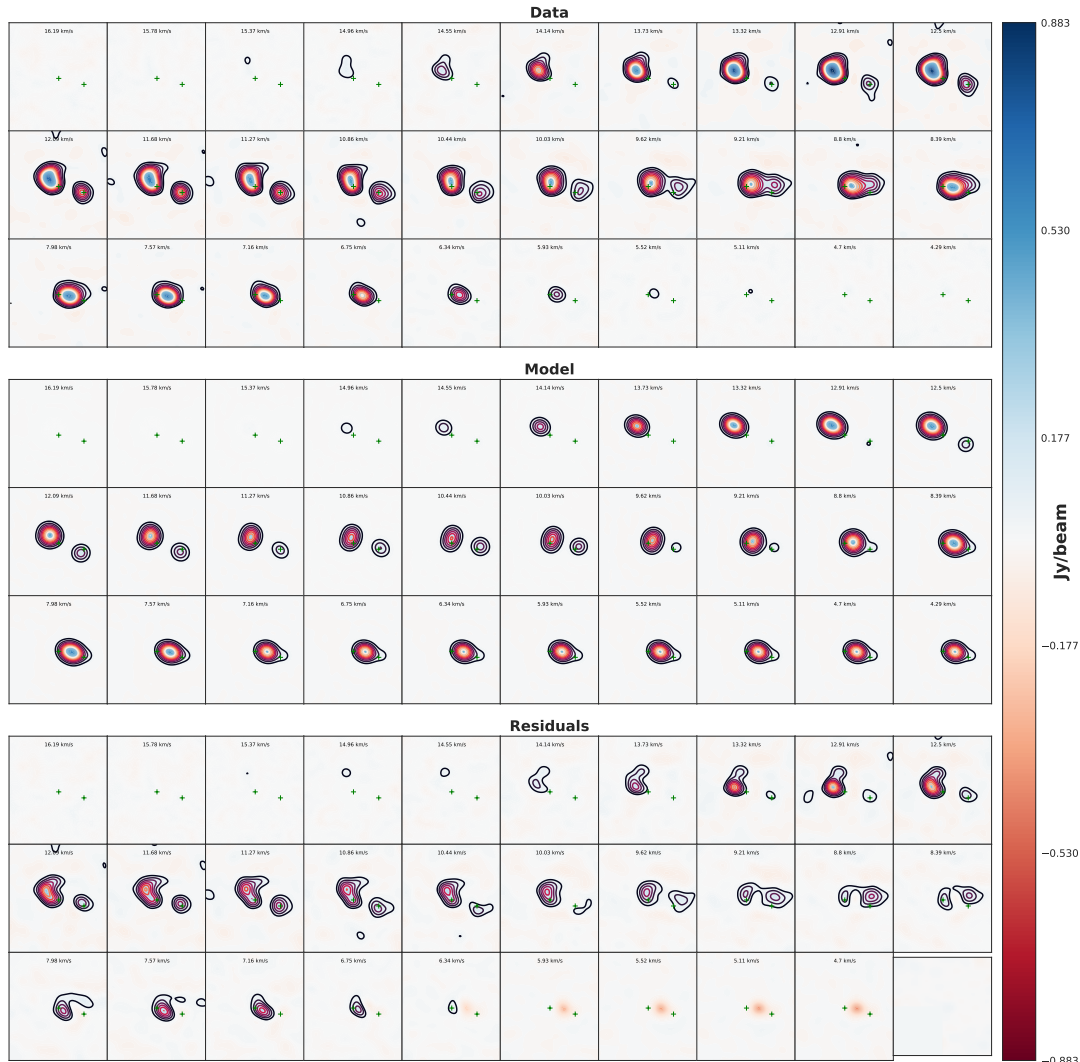


Figure 1.4: Channel maps of HCO⁺ emission data, as well as a best-fit model from MCMC fitting and residuals from the two.

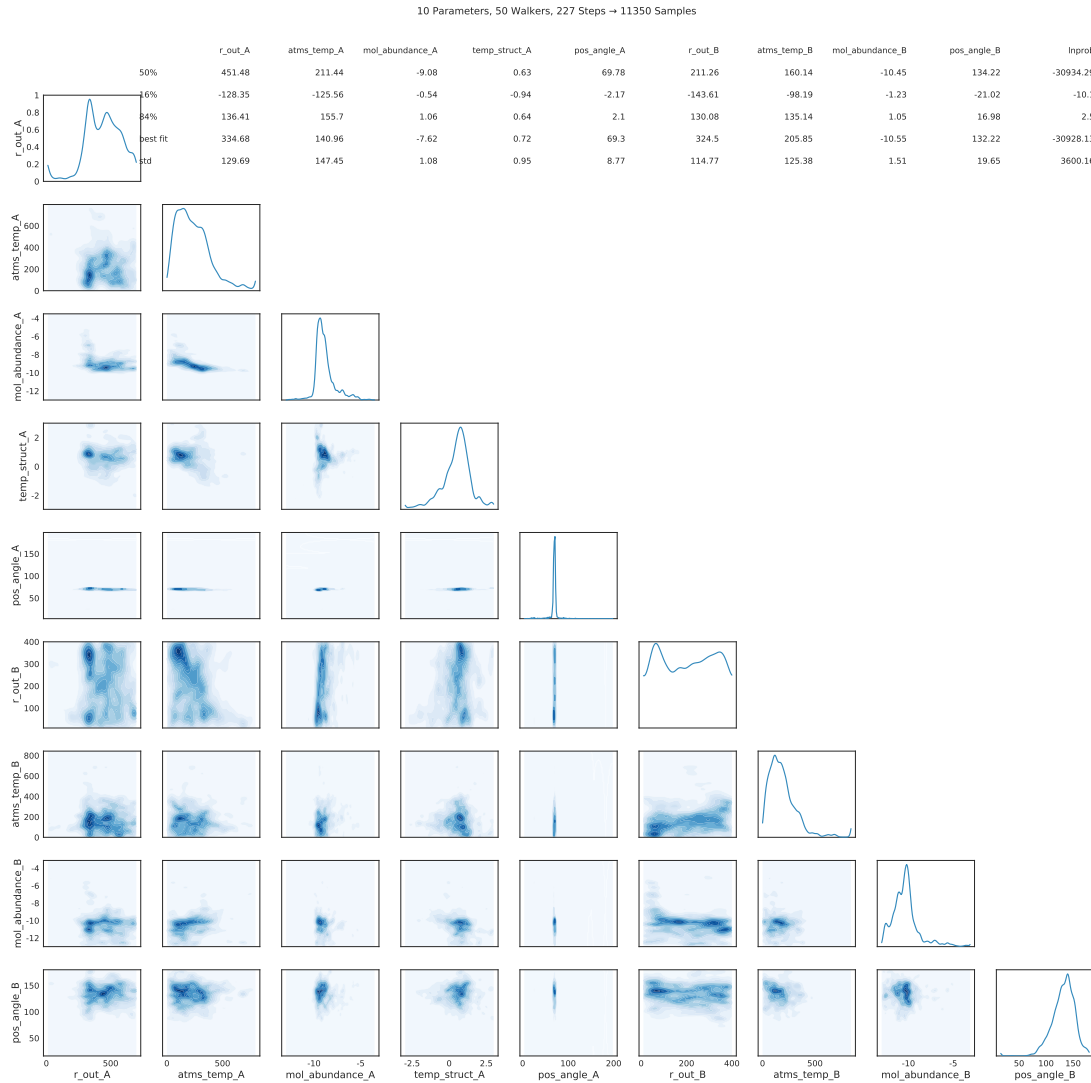


Figure 1.5: Cornerplots of results from MCMC fitting of HCN emission.

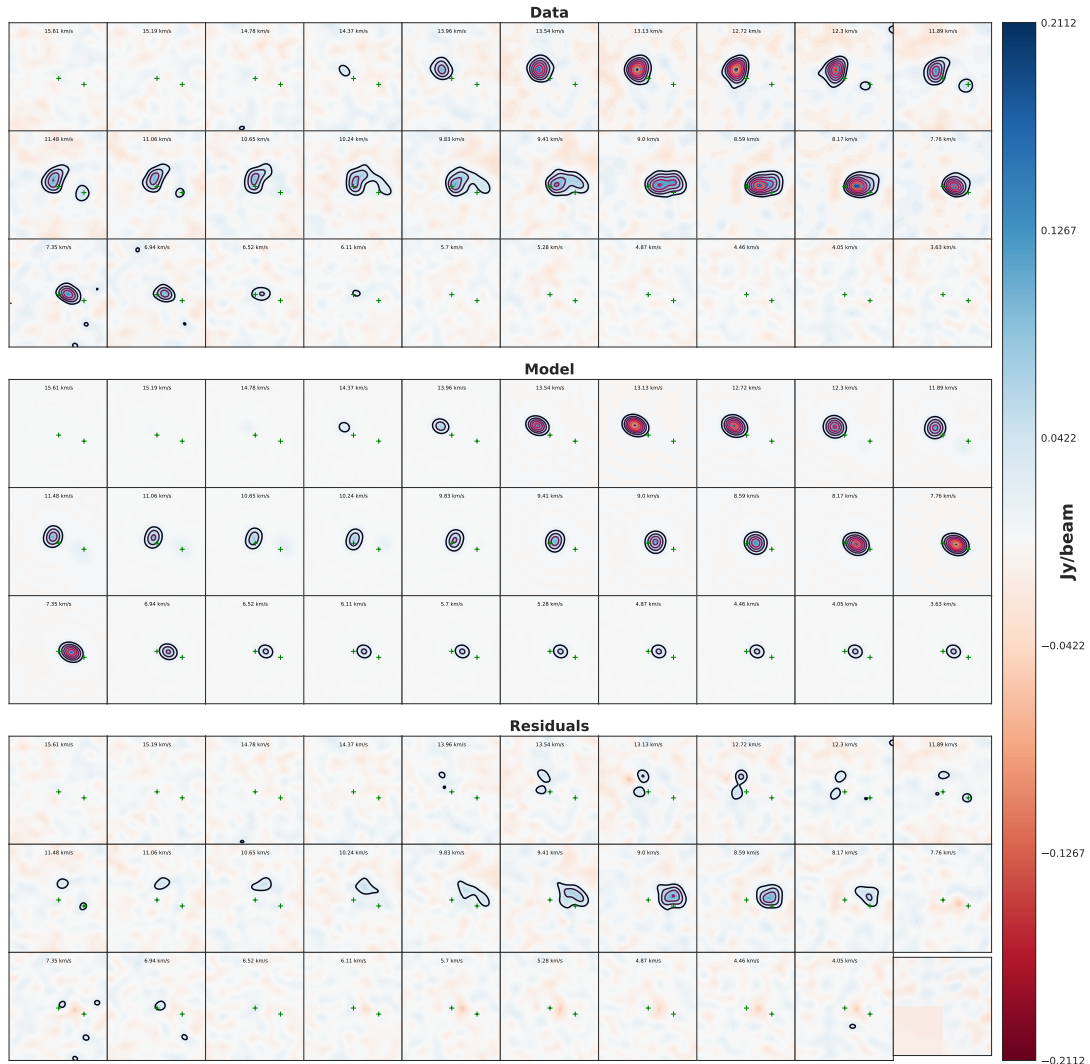


Figure 1.6: Channel maps of HCO⁺ emission data, as well as a best-fit model from MCMC fitting and residuals from the two.

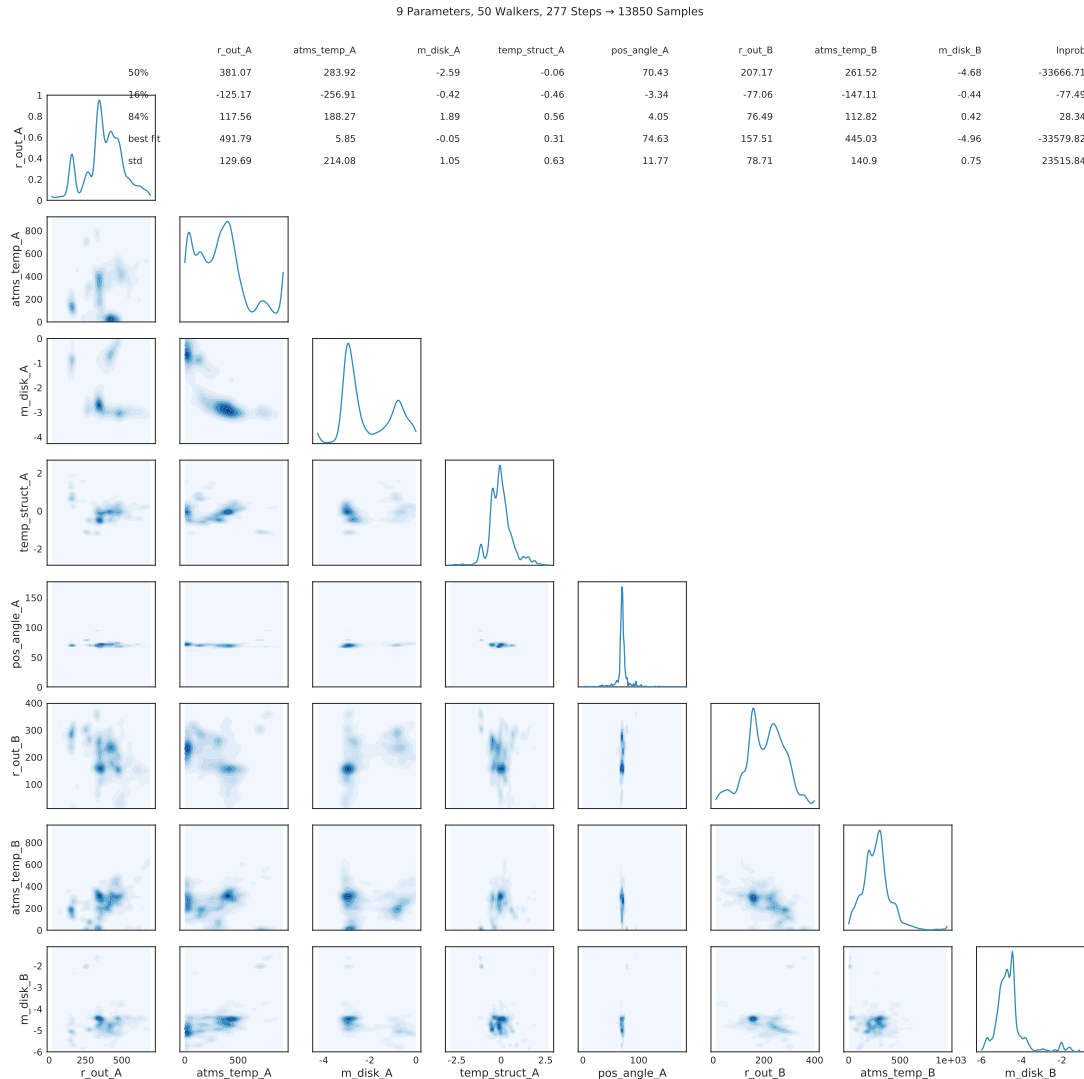


Figure 1.7: Cornerplots of results from MCMC fitting of HCN emission.

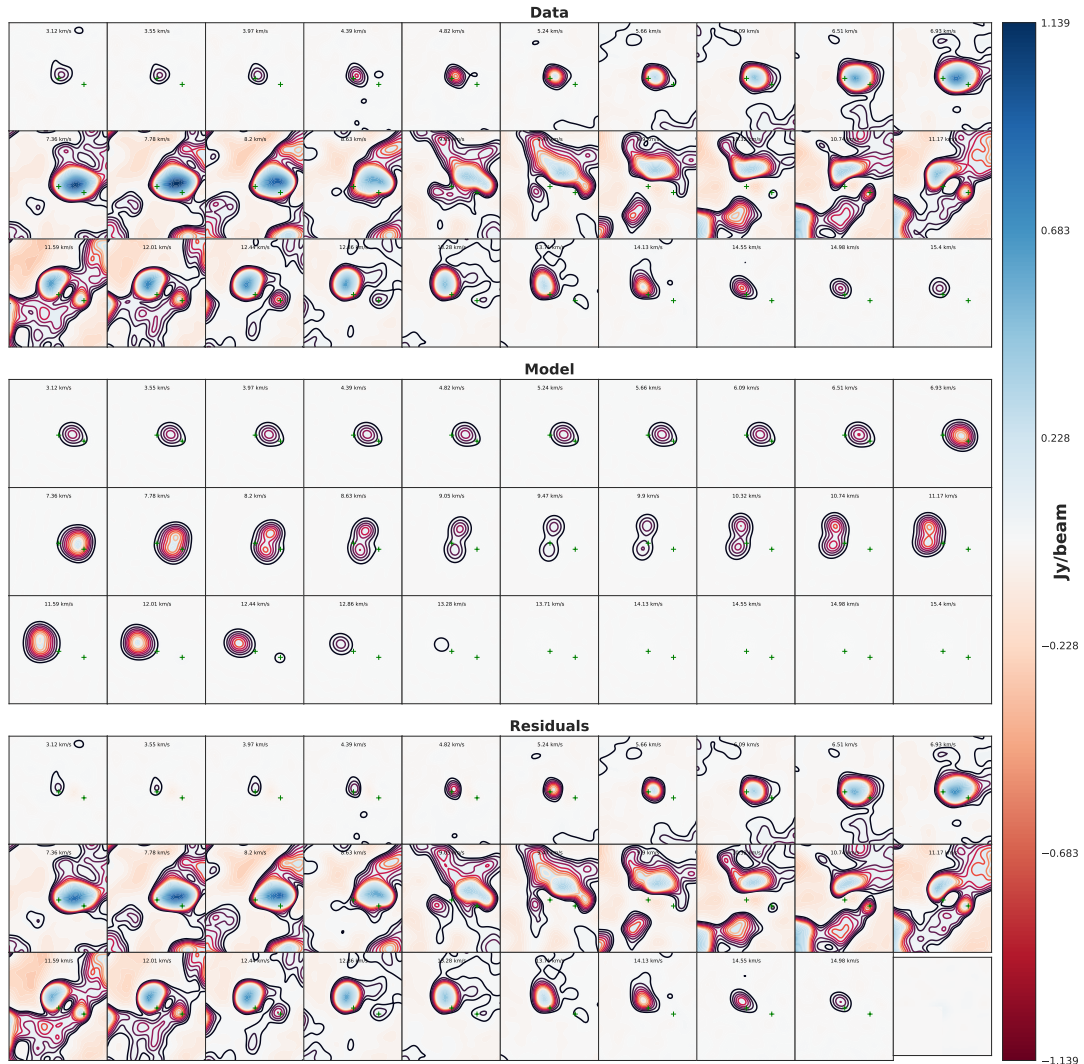


Figure 1.8: Channel maps of HCO^+ emission data, as well as a best-fit model from MCMC fitting and residuals from the two.

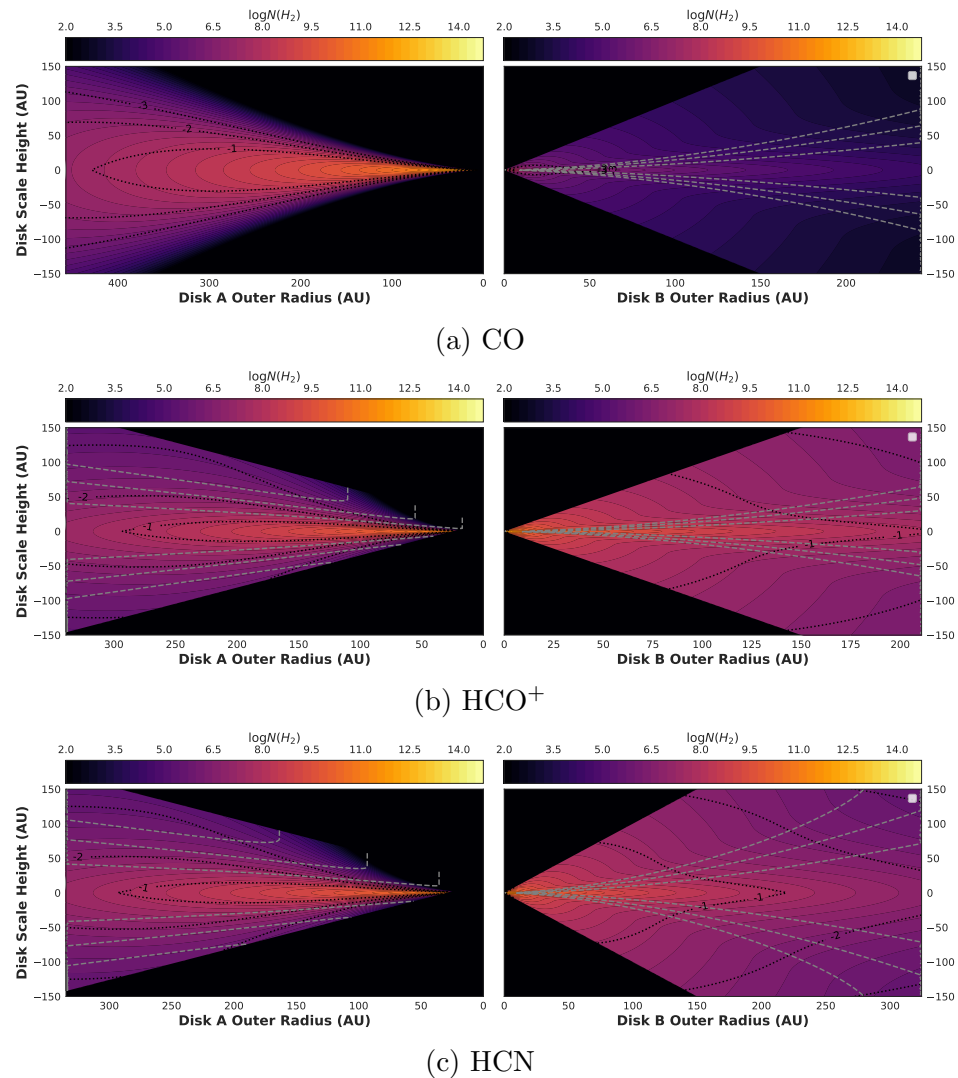


Figure 1.9: Density and temperature profiles for the best-fit models for CO, HCO^+ , and HCN.

Chapter 2

Discussion

With the disks now fit, we may interpret our results. Since this project was based around the question of how environment influences protoplanetary disks, we would like to compare our best fit values to other disks, including both those also in the ONC (Factor et al. 2017) and outside of it, as well as to modeling efforts. We also view our results in the context of planet formation potential, and maybe discuss some other stuff, too.

2.1 Reflections on the Fits

Looking at the fits to our three molecular lines side by side, several things jump out. First and foremost, as discussed in §??, our attempts to fit the CO line were overwhelmed by the significant cloud contamination around the disk. If this run had converged, we would have used its disk mass results in the other runs, but since these results are not to be trusted, we instead continued to use the disks' mass values presented in Williams et al. (2014), which were inferred from continuum emission.

The HCO⁺ and HCN runs converged into impressive agreement, although their posteriors show that HCO⁺ line resulted in a much more confident model. Both lines show surprisingly high chemical abundances in disk A, while both also show significantly lower values for disk B abundances (discussed below). Additionally,

the two lines' fits for outer radius agree to within around 1% (although the HCN fit is significantly less certain than the HCO^+ fit) and the lines' best-fit q values agree to within 15%. Atmospheric temperatures for disk A in both lines are large and significantly different, with the HCO^+ line preferring a temperature 50% greater than HCN's, but this is at least somewhat expected, as the two molecules are emitting from different regions of the disk. In both lines, disk A's temperature structure power law index, q , is decidedly positive, although we expect this parameter to not settle with absolute certainty on a single value, since the observations don't have enough spatial resolution to constrain it tightly.

Fits for disk B are systematically far less well constrained, since it is smaller, unresolved, and more easily overrun by excess emission from disk A, the connecting feature between the disks, and cloud contamination. Still, save for the disk's outer radius fit, all parameters are within reason, although the atmospheric temperature in the HCN line is notably high.

As discussed in §1.3.2, a posteriori cuts of the HCN fit's MCMC chain limiting disk B's outer radius to not exceed 220 AU changes the best-fit parameters significantly, most notably leading the fits of disk B's outer radius in HCO^+ and HCN into agreement and pushing disk A's HCN abundance more than a full order of magnitude higher.

Whether this is a reasonable cut is not yet clear to me.

The HCN line chanmaps show a really strong connection between disks around $v=10.24, 9.83$. Maybe it's just disk B reappearing, but the connector seems a lot stronger in this line than in HCO^+ . Does this reflect their different emitting regions?

2.2 Comparison with the Literature

? we compare our results to those from other studies that have modeled line emission from protoplanetary disks. The most immediately relevant of these is the work by Factor et al. (2017), in which they use a similar modeling technique to characterize another ONC proplyd from the same survey as our binary, and thus represent the only other disk studied in this way that is also in a high-mass star forming region. The others are well-studied disks in low-mass regions. We may compare our temperature profiles and abundance to these other systems and look for variations from expected values.

Comparing our results for disk A to these other studies, we can see that our atmospheric temperatures in $\text{HCO}^+(4-3)$ and $\text{HCN}(4-3)$ are consistent with the results of the HCO^+ fit in Factor et al. (2017). They are, however, significantly higher than any other study's fit.

Additionally, our temperature structures are systematically positive, reflecting a temperature structure that increases with radius. As with the atmospheric temperature, this is contrasted by all other results, which have moderately negative values, save that of the Factor et al. (2017) HCO^+ line, which is also positive, but less dramatic than in our fits. These positive values stand in contrast to the expected q value of $-0.5^{+0.2}_{-0.1}$ for a geometrically flat, optically thin disk (Dartois et al. 2003). *Rosenfeld2012 (on V4046) report q=0.63,*

Is the exponent in these temp eqns universally (-q) or does the minus sometimes get swallowed up? - ζ Does a positive q correspond to a decreasing radial temp? Dartois2003, Rosenfeld2012, Hughes2008 have that; unclear for Kevin's code.

It is (seems?) possible that these discrepancies in q and X_{mol} could reflect the fact that our fits had different values for some of the fixed parameters. These

Table 2.1: Disk Parameter List

Reference	Source	Line	q	$\log X_{\text{mol}}$	Atms.	Temp
This study	d253-1536a	$\text{HCO}^+(4-3)$	0.66	-7.96	151	
	d253-1536a	$\text{HCN}(4-3)$	0.72	-7.62	140	
	d253-1536a	$\text{CO}(3-2)^{\text{a}}$	0.40	[-4]	1	
Factor et al. (2017)	d216-0939	$\text{HCO}^+(4-3)$	0.17	-10.08	190	
	d216-0939	$\text{CO}(3-2)$	-0.33	[-4]	70	
	d216-0939	$\text{HCN}(4-3)$	-0.18	-6.7	19	
Flaherty et al. (2015)	HD163296	$\text{CO}(3-2)$	-0.22	[-4]	94	
	HD163296	$\text{CO}(2-1)$	-0.27	[-4]	79	
Hughes et al. (2008) ^b	A bunch	$\text{CO}(3-2)$	-	[-4]	-	
Rosenfeld et al. (2012) ^b	V4046 Sgr	$^{12}\text{CO}(2-1)$	0.63	[-4]	-	
Flaherty et al. (2017) ^c	HD163296	$\text{DCO}^+(3-2)$	[-2.22]	-10.79	[94]	
Zhang et al. (2017)	TW Hya	$^{13}\text{C}^{18}\text{O}(3-2), \text{C}^{18}\text{O}(3-2)$	-0.47	-7.96	151	
Flaherty et al. (2018) ^d	TW Hya	$\text{CO}(6-5, 3-2, 2-1)$	-0.46	[-4]	31	

^{*} Since there is not a convention about whether a negative value of q indicates a radially decreasing or increasing temperature structure (in other words, whether or not q is implicitly negative), some of these values have the opposite sign of the value reported in their article. When this is the case, it indicates that, in that original paper, atmospheric temperature was defined such that $T_{\text{atms}} \propto T_0^{-q}$. In our work, and in all the values given here, it is the case that $T_{\text{atms}} \propto T_0^q$, meaning that a negative value of q leads to temperature decreasing with radius.

^{**} Values in [brackets] were fixed during fitting.

^a This result is being presented for completeness (and to allow for the chance that something changes dramatically in coming runs REWORK), but since its T_{atms} clearly got stuck, it is not a useful result for comparison and will not be discussed.

^b Rosenfeld et al. (2012) didn't fit for T_{atms}

^c In Flaherty et al. (2017), they fit three rings, and consequently have three slightly different values for each parameter. The values reported here are for their middle ring, although the three do not vary significantly from one another. Additionally, T_{atms} and q were fixed at values found for CO(3-2) in Flaherty et al. (2015), and only X_{mol} was fit for.

^d Flaherty et al. (2018) developed several models, with different morphological structures. The results presented here are drawn from their simplest (fiducial) model.

include R_{crit} , which we fix at 100 and Sam fixed at 600 AU, as well as z_q and T_{mid} ¹, which they fit for by simultaneously fitting CO and HCO⁺emission and yielding values of $z_{q,150} = 73$ AU and $T_{mid} = 24.7$ K, in comparison to our values of 29 and 19, respectively.

Is this enough to make an appreciable difference? I don't know. It seems most likely to me that those drastically different R_C values could explain the different q values, since if my disks are having their densities killed way earlier, then maybe they're struggling to match the flux levels further out.

Another question about Sam's work: His paper and thesis have different values for the HCO⁺ and CO fits. He also makes no mention of the multi-line fits in his paper, which seems weird.

Our molecular abundances for each disk are vary widely from those reported in the Factor et al. (2017) paper, the only other study to model HCO⁺emission². In it, they report finding canonical values for the HCO⁺line ($\log X_{HCO^+} = -10.04$) and an unexpectedly high values for the HCN line ($\log X_{HCN} = -6.7$). However, we find that, while both lines' disk B fits hover in the range of -10, disk A shows an appreciably higher abundance in both lines of $\log X_{mol} \approx -8$.

We may also compare these abundances to theoretical modeling efforts. Walsh et al. (2010) developed radial and vertical chemical models for an imaginary isolated protoplanetary disk around a T-Tauri star, studying molecular abundance distributions throughout the disk for molecules within ALMA's reach. They showed that log abundances in their models for HCO⁺varied from -8 to -12, -7 to -12 for HCN, and -4 to -9 for CO (see Fig. ??).

The authors then built on this model by adding robust modeling of externally-

¹Since Sam fit multiple lines simultaneously, they were able to constrain these parameters, which is not possible in the case of single-line fitting.

²This probably isn't true; someone else must've done it before.

driven UV and X-ray ionization (Walsh et al. 2012) and applying it to another imaginary protoplanetary disk around a T-Tauri star, this time with an O star nearby providing ionizing photons (Walsh et al. 2013). They then make the same molecular abundance distribution maps as before.

The authors note that, in their model photoionized disk, HCO^+ column density increases by a factor of 6.3 relative to the isolated disk, whereas HCN and CO column densities remain constant through ionization. This would be useful if we had an estimation of what the HCO^+/HCN ratio would be in an isolated disk. Is Table 6 in Walsh2013 giving that? Sam said that an HCO^+/HCN value above or below unity was indicative of something, but I'm really not seeing that.

They also note that the ionized disks have much higher gas temperatures, \gg 50 K. This is consistent with our findings.

While our modeling assumes a constant chemical abundance across the whole disk, these models provide a sanity check, confirming that our results are within the predicted ranges, despite the fact that the HCO^+ abundance is significantly higher than the value predicted by other studies.

It is probably also worth at least mentioning that these disks are rather atypically large. A survey of Lupus disks (Cieza et al. 2019) showed none with radii greater than 30 AU (double check this number), and smaller masses. Might be useful to put their Fig. 13 (of disk mass) in here, adding points to show where these disks are. Maybe mass/radius should be something that gets discussed more in general here?

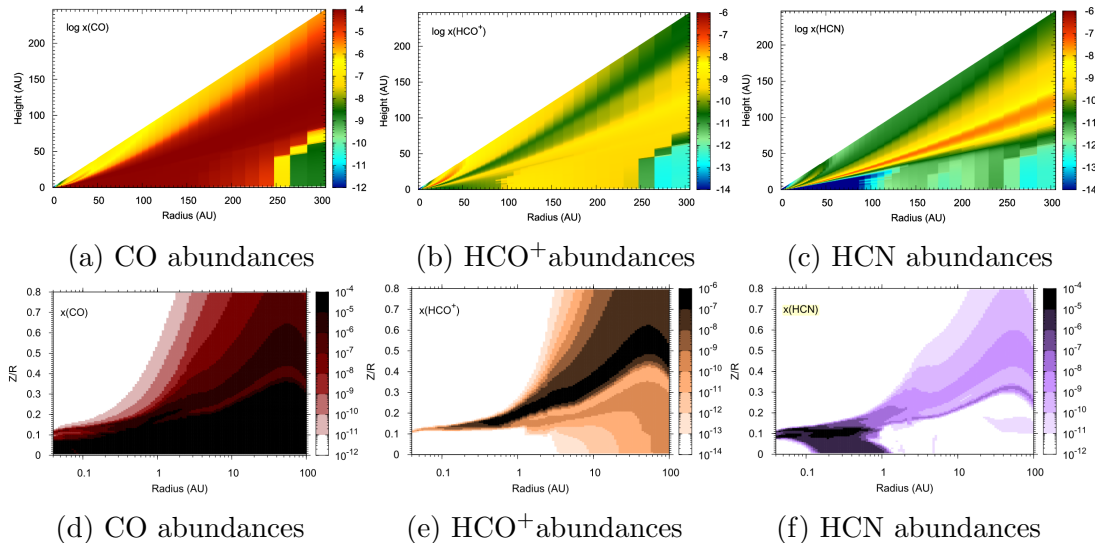


Figure 2.1: Models from Walsh et al. (2013) showing radial and vertical distributions of CO, HCO^+ , and HCN in a simulated disk around a T-Tauri star, being radiated by a nearby O star. The top row shows the profiles of isolated disks (Walsh et al. 2010), while the bottom row shows the profiles of disks being irradiated by a nearby O star (Walsh et al. 2013). Note that bottom row is on a log scale and only covers the inner 100 AU of the disk, while the top row is linearly scaled and shows a 300AU stretch. *It seems like only having one of these sets of images would make more sense.*

2.3 Formation of the Binary

This seems consistent with the hypothesis, based on the wide separation of the binary's components, that these disks may have formed separately, in regions with different chemistries, and drifted together later. Maybe?

Williams et al. (2014) note that previous works on wide binaries (??) have indicated that these pairs likely do not form together in the same large, co-rotating structures.

2.4 Planet-Forming Potential

One way to contextualize the results presented in §1 is through the lens of planet formation. This analysis traditionally begins with a comparison to the MMSN, which is the density profile that our own Solar System would have if all our planets had gas added to them until their composition matched that of the Sun, then each planet's mass was spread out in a ring along its orbital path (as discussed in §??). Integrating this mass leaves us with $M_{\text{MMSN}} \approx 0.01M_{\odot}$. It is worth reiterating that this is an extremely rough metric, build on several assumptions, and that it does not reflect *minimum* mass of a planet forming potential, but rather an approximation of the mass it would take for a disk like ours to form.

With the extremely large mass of $M = 0.36M_{\odot}$ that we measure in the CO line, it is needless to say that the disk's mass would not be its limiting factor in planet formation.

Bibliography

- Aikawa, Y., & Herbst, E. 2003, *Astron. Astrophys.*, 371, 1107
- Anderson, K. R., Adams, F. C., & Calvet, N. 2013, *Astrophys. J.*, 774
- Andrews, S. M., et al. 2018, *Astrophys. J. Lett.*
- Andrews, S. M., & Williams, J. P. 2005, *Astrophys. J.*, 631, 1134
- . 2007, *Astrophys. J.*, 1
- Andrews, S. M., Wilner, D. J., Hughes, A. M., Qi, C., & Dullemond, C. P. 2009, *Astrophys. J.*, 700, 1502
- Ansdell, M., Williams, J. P., Manara, C. F., Miotello, A., Facchini, S., van der Marel, N., Testi, L., & van Dishoeck, E. F. 2017, *Astron. J.*, 153, 240
- Bontemps, S., et al. 2001, *Astron. Astrophys.*
- Bosman, A. D., van Dishoeck, E. F., & Walsh, C. 2018, *Astron. Astrophys.*
- Butler, B. 2012, ALMA Memo 594
- Chiang, E., & Laughlin, G. 2013, *Mon. Not. R. Astron. Soc.*, 431, 3444
- Cieza, L. A., et al. 2019, *Mon. Not. R. Astron. Soc.*, 482, 698
- Cleeves, L. I., Bergin, E. A., & Adams, F. C. 2014, *Astrophys. J.*, 794
- Cleeves, L. I., Bergin, E. A., Bethell, T. J., Calvet, N., Fogel, J. K. J., Sauter, J., & Wolf, S. 2011a, *Astrophys. J. Lett.*, 743, 1
- . 2011b, *Astrophys. J. Lett.*, 743, 1

- Collaboration, T. E. H. T. 2019, *Astrophys. J.*, 1
- Combes, F., et al. 2018, *Astron. Astrophys.*, 79, 1
- Dartois, E., Dutrey, A., & Guilloteau, S. 2003, *Astron. Astrophys.*, 399, 773
- de Gregorio-Monsalvo, I., et al. 2013, *Astron. Astrophys.*, 557, A133
- Duchêne, G., & Kraus, A. 2013, *Annu. Rev. Astron. Astrophys.*, 1
- Dullemond, C. P., & Monnier, J. D. 2010, *Annu. Rev. Astron. Astrophys.*, 1
- Eisner, J. A., et al. 2018, *Astrophys. J.*
- Eistrup, C., Walsh, C., & van Dishoeck, E. F. 2017, *Astron. Astrophys.*
- F. Shu, F. Adams, S. L. 1987, *Annu. Rev. Astron. Astrophys.*
- Factor, S. M., et al. 2017, *Astrophys. J.*
- Flaherty, K. M., et al. 2017, 163296, 1
- Flaherty, K. M., Hughes, A. M., Rosenfeld, K. A., Andrews, S. M., Chiang, E., Simon, J. B., Kerzner, S., & Wilner, D. J. 2015, *Astrophys. J.*, 813, 1
- Flaherty, K. M., Hughes, A. M., Teague, R., Simon, J. B., Andrews, S. M., & Wilner, D. J. 2018, 1
- Fogel, J. K., Bethell, T. J., Bergin, E. A., Calvet, N., & Semenov, D. 2011, *Astrophys. J.*, 726
- Foreman-mackey, D., Hogg, D. W., Lang, D., & Goodman, J. 2013, *Publ. Astron. Soc. Pacific*
- Gaia Collaboration. 2016, *Astron. Astrophys.*

- Gaia Collaboration, Brown, A. G. A., Vallenari, A., Prusti, T., de Bruijne, J. H. J., Babusiaux, C., & Bailer-Jones, C. A. L. 2018, *Astron. Astrophys.*
- Gaidos, E., Krot, A. N., Williams, J. P., & Raymond, S. N. 2009, *Astrophys. J.*, 696, 1854
- Goodman, J., & Weare, J. 2010, *Math. Sci. Publ.*, 5, 1
- Hartmann, L., Calvet, N., Gullbring, E., & D'Alessio, P. 1998, *Astrophys. J.*, 741
- Haworth, T. J., Boué, D., Facchini, S., Bisbas, T. G., & Clarke, C. J. 2016, *Mon. Not. R. Astron. Soc.*, 463, 3616
- Henney, W. J., & O'Dell, C. R. 1999, *Astron. J.*, 118, 2350
- Herrera-Martín, A., Hendry, M., Gonzalez-Morales, A. X., & Ureña-López, L. A. 2019, *Astrophys. J.*, 872, 11
- Hildebrand, R. 1983, *Q. J. R. Astron. Soc.*, 24, 267
- Hogbom, J. 1974, *Astron. Astrophys. Suppl.*
- Hubickyj, O., Bodenheimer, P., & Lissauer, J. J. 2005, *Icarus*, 179, 415
- Hughes, A. M. 2010, PhD thesis, Harvard University
- Hughes, A. M., Duchene, G., & Matthews, B. 2018, *Annu. Rev. Astron. Astrophys.*, 1
- Hughes, A. M., et al. 2017, *Astrophys. J.*, 839, 86
- Hughes, A. M., Wilner, D. J., Qi, C., & Hogerheijde, M. R. 2008, *Astrophys. J.*
- Jensen, E. L., & Akeson, R. 2014, *Nature*, 511, 567

- Johnstone, D., Hollenbach, D., & Bally, J. 1998, *Astrophys. J.*, 499, 758
- Kalyaan, A., Desch, S. J., & Monga, N. 2015, *Astrophys. J.*, 815, 112
- Kenyon, S. J., Gomez, M., & Whitney, B. A. 2008, *Handb. Star Form. Reg.* Vol. I, I
- Kruijssen, J. M. D., & Longmore, S. N. 2019, 1
- Kuchner, M. J. 2004, *Astrophys. J.*, 612, 1147
- Lada, C. J., & Lada, E. A. 2003, *Annu. Rev. Astron. Astrophys.*, 57
- Liu, Y., et al. 2018, 75, 1
- Luhman, K. L., Allen, P. R., Espaillat, C., Hartmann, L., & Calvet, N. 2010, *Astrophys. Journal, Suppl. Ser.*, 186, 111
- Lynden-Bell, D., & Pringle, J. E. 1974, *Mon. Not. R. Astron. Soc.*, 168, 603
- Mann, R. K., Andrews, S. M., Eisner, J. A., Williams, J. P., Meyer, M. R., Di Francesco, J., Carpenter, J. M., & Johnstone, D. 2015, *Astrophys. J.*, 802, 1
- Mann, R. K., et al. 2014, *Astrophys. J.*, 784, 1
- Mann, R. K., & Williams, J. P. 2009, *Astrophys. J.*, 699, 1994
- McKee, C. F., & Ostriker, E. C. 2007, *Annu. Rev. Astron. Astrophys.*, 565
- McMullin, J. P., Waters, B., Schiebel, D., Young, W., & Golap, K. 2007, *Astron. Soc. Pacific Conf. Ser.*, 376, 127
- Miotello, A. 2017, *Proc. Int. Astron. Union*, 13, 124
- Observatory, A. ????, *Origins — ALMA*

- Ovelar, M. d. J., Kruijssen, J. M. D., Bressert, E., Testi, L., Bastian, N., & Cabrera, H. C. 2012, 1, 1
- Pavlyuchenkov, Y., Semenov, D., Henning, T., Guilloteau, S., Pietu, V., Launhardt, R., & Dutrey, A. 2007, *Astrophys. J.*, 669, 1262
- Podio, L., et al. 2019, *Astron. Astrophys.*, 6, 1
- Qi, C., D'Alessio, P., Berg, K. I., Wilner, D. J., Hughes, A. M., Andrews, S. M., & Ayala, S. 2011, *Astrophys. J.*, 740
- Raymond, S. N., & Cossou, C. 2014, *Mon. Not. R. Astron. Soc. Lett.*, 440
- Reboussin, L., Wakelam, V., Guilloteau, S., Hersant, F., & Dutrey, A. 2015, *Astron. Astrophys.*, 579, A82
- Reggiani, M., Robberto, M., Da Rio, N., Meyer, M. R., Soderblom, D. R., & Ricci, L. 2011, *Astron. Astrophys.*, 534, A83
- Ricci, L., Robberto, M., & Soderblom, D. R. 2008, *Astron. J.*, 136, 2136
- Ricci, L., Testi, L., Williams, J. P., Mann, R. K., & Birnstiel, T. 2011, *Astrophys. J. Lett.*, 739, 1
- Robberto, M., et al. 2013, *Astrophys. Journal, Suppl. Ser.*, 207
- Rosenfeld, K. A., Andrews, S. M., Hughes, A. M., Wilner, D. J., & Qi, C. 2013, *Astrophys. J.*, 774
- Rosenfeld, K. A., Andrews, S. M., Wilner, D. J., & Stempels, H. 2012, *Astrophys. J.*, 806

- Sault, R. J., Teuben, P. J., & Wright, M. C. H. 1995, Astron. Data Anal. Softw. Syst.
- Schöier, F. L., van der Tak, F. F. S., van Dishoeck, E. F., & Black, J. H. 2005, Astron. Astrophys., 432, 369
- Schwarz, K. R., Bergin, E. A., Cleeves, L. I., Blake, G. A., Zhang, K., Öberg, K. I., van Dishoeck, E. F., & Qi, C. 2016, Astrophys. J., 0, 1
- Skilling, J., & Bryan, R. K. 1984, Mon. Not. R. Astron. Soc., 211, 111
- Smith, N., Bally, J., Licht, D., & Walawender, J. 2005, Astron. J., 129, 382
- Tachibana, S., Huss, G. R., Kita, N. T., Shimoda, G., & Morishita, Y. 2006, Astrophys. J., 639, L87
- Tsiganis, K., Gomes, R., Morbidelli, A., & Levison, H. F. 2005, Nature, 435, 459
- van Dishoeck, E. F., & Blake, G. A. 1998, Astron. Astrophys.
- Vicente, S. M., & Alves, J. 2005, in Astron. Astrophys., Vol. 205, 214–216
- Walsh, C., et al. 2016, Astrophys. J., 823, L10
- Walsh, C., Millar, T. J., & Nomura, H. 2010, Astrophys. J., 722, 1607
- . 2013, Astrophys. J. Lett., 766, 1
- Walsh, C., Nomura, H., Millar, T. J., & Aikawa, Y. 2012, Astrophys. J., 747
- Walsh, K. J., Morbidelli, A., Raymond, S. N., O'Brien, D. P., & Mandell, A. M. 2011, Nature, 475, 206
- Weidenschilling, S. 1977, Astrophys. Space Sci.

- Wernecke, S. J., & D'Addario, L. R. 1977, IEEE Trans. Signal Process., 39, 1478
- Williams, J. P., & Best, W. M. J. 2014, *Astrophys. J.*, 788
- Williams, J. P., & Cieza, L. A. 2011, *Astrophys. J.*
- Williams, J. P., et al. 2014, *Annu. Rev. Astron. Astrophys.*, 796
- Xiao, L., & Chang, Q. 2018, *Astrophys. J.*, 853, 22
- Yu, M., Evans, N. J., Dodson-Robinson, S. E., Willacy, K., & Turner, N. J. 2017,
Astrophys. J., 1
- Zhang, K., Bergin, E. A., Blake, G. A., Cleeves, L. I., & Schwarz, K. R. 2017,
Nat. Astron., 1